Imaging phase segregation in nanoscale Li_xCoO_2 single particles

Elliot J. Fuller[1], David S. Ashby[1], Celia Polop[2,3], Elena Salagre[2], Bhuvsmita Bhargava[4], Yueming Song[4], Enrique Vasco[5], Joshua D. Sugar[1], Paul Albertus[4], Tevfik Onur Menteş[6], Andrea Locatelli[6], Pilar Segovia [2,3], Miguel Ángel Gonzalez-Barrio[7], Arantzazu Mascaraque[7], Enrique G. Michel[2,3] and A. Alec Talin[1]**

[1]Sandia National Laboratories, 7011 East Ave. Livermore, CA 94550, USA

[2]Departamento de Física de la Materia Condensada and Instituto Universitario de Ciencia de Materiales Nicolás Cabrera (INC), Universidad Autónoma de Madrid, 28049 Madrid, Spain

[3] IFIMAC (Condensed Matter Physics Center), Universidad Autónoma de Madrid, 28049 Madrid, Spain

[4]Department of Chemical and Biomolecular Engineering, University of Maryland, College Park, MD, 20740, USA

[5]Instituto de Ciencia de Materiales de Madrid, CSIC, Sor Juana Inés de la Cruz 3, 28049 Madrid, Spain

[6]Sincrotrone Trieste S.C.p.A., Basovizza, Trieste 34149, Italy

[7] Departamento de Física de Materiales, Universidad Complutense de Madrid, 28040 Madrid, Spain

KEYWORDS

intercalation oxides, conductive atomic force microscopy, photoemission electron microscopy, phase separation

ABSTRACT

Li_xCoO_2 (LCO) is a common battery cathode material that has recently emerged as a promising material for other applications including electrocatalysis(*1, 2*) and as electrochemical random access memory (ECRAM)(*3*). During charge-discharge cycling LCO exhibits phase transformations that are significantly complicated by electron correlation. While the bulk phase diagram for an ensemble of battery particles has been studied extensively, it remains unclear how these phases scale to nanometer dimensions and the effects of strain and diffusional anisotropy at the single particle scale. Understanding these effects is critical to modeling battery performance and for predicting the scalability and performance of electrocatalysts and ECRAM. Here we investigate isolated, epitaxial $LiCoO_2$ islands grown by pulsed laser deposition (PLD). After electrochemical cycling of the islands, conductive atomic force microscopy (c-AFM) is used to image the spatial distribution of conductive and insulating phases. Above 20 nm island thicknesses, we observe a kinetically arrested state in which the phase boundary is perpendicular to the Li-planes; we propose a model and present image analysis results that show smaller LCO islands have a higher conductive fraction than larger area islands, and the overall conductive fraction is consistent with lithiation state. Thinner islands (14 nm), with a larger surface to volume ratio, are found to exhibit a striping pattern which suggests surface energy can dominate below a critical dimension. When increasing force is applied through the AFM tip to strain the LCO islands, significant shifts in current flow are observed, and underlying mechanisms for this behavior are discussed. The c-AFM images are compared with photoemission electron microscopy (PEEM) images which are used to acquire statistics across hundreds of particles. The results indicate that strain and morphology become more critical to electrochemical performance as particles approach nanometer dimensions.

INTRODUCTION

Understanding and controlling phase transformations and local electronic properties is important for various electrochemical energy storage, energy conversion and emerging information processing applications. For batteries, the phase equilibrium determines the open circuit voltage. Moreover, phases with drastically different electronic and ionic transport characteristics will charge at different rates, leading to reduced overall capacity(*1*). For electrocatalysts, phases with distinct surface atomic and electronic structures can have considerably different activity, selectivity and stability(*2, 3*). For ECRAM, the electronic conductivity of an LCO channel, reversibly tuned by Li ion insertion, represents a memory state(*4, 5*). Understanding the conductive phase morphology at a length scale of tens of nanometers is therefore critical to developing high density memory devices. However, a clear relationship between LCO particle size, diffusional anisotropy and strain on the resulting phase morphology has yet to be established.

In the layered, rhombohedral form of LCO (space group $R\underline{3}m$), monovalent cations (Li^+) are accompanied by a formally trivalent oxidation state of Co^{3+} with O^{2-} oxygen anions. The extraction of Li^+ in Li_xCoO_2 changes the oxidation state from Co^{3+} to Co^{4+} and results in reversible changes to the electronic and structural properties over the range $0.5<x<1.0$(*6, 7*). Stoichiometric LCO is a band insulator that should become metallic once a small fraction of lithium is extracted ($x<1.0$), but remains insulating due to electron correlation and/or disorder induced carrier localization(*8, 9*). LCO is an insulator at compositions $0.96<x<1$, while at compositions $x<0.75$ it is metallic. At fractions $0.75<x<0.94$, LCO exhibits a two-phase regime where insulating α-phase and a metallic β-phases coexist.

Previous efforts have focused on interrogating the structural and electronic properties of ensembles of LCO particles immersed in binder and liquid electrolyte(*9, 10*). In these studies, it

remains unclear whether all particles exist in similar microscopic states with equal fractions of insulating and metallic domains between $0.75<x<0.94$, or whether certain particles share a larger fraction of electrochemical activity during charge and discharge(*11-13*). This has direct implications to ECRAM and battery performance, wherein certain particles could potentially dominate the device properties due to higher metallicity and a larger electrochemical activity.

Single particle studies are more challenging due to the strong orientation dependence of diffusion in LCO and the nanoscopic nature of the phase domains. For example, Zhu *et. al*. carried out electrochemical delithiation of an LCO grain in a polycrystalline film using a c-AFM tip(*14*). However, the phase boundaries could not be clearly resolved, the particle orientation was uncertain, and it is unclear whether the tip-induced delithiation used in the experiment is equivalent to electrochemical cycling. Past efforts to image the local state of charge (SOC) of individual LCO particles measuring several microns in diameter using scanning transmission x-ray microscopy (STXM) showed considerable inhomogeneity(*15*). However, the TXM measurements, with a reported spatial resolution of ~90 nm, did not reveal how the variations in the SOC were associated with the α- and β-phases. More recently, optical interferometric scattering microscopy was used to measure phase dynamics during charge-cycling of 10 micron sized particles(*16*). Still, the large particle size and diffraction limited spatial resolution (reported at 280 nm) inhibited studying nanoscale particles and features. The ability to resolve phase domains across clearly oriented, nanoscale particles is needed. Therefore, we have carried out a high-resolution microscopy study of phase domains in oriented, nanoscale islands using both c-AFM and PEEM.

EXPERIMENTAL

We used PLD to grow epitaxial $LiCoO_2$ on $SrTiO_3$ substrates with a metallic $SrRuO_3$ underlayer as established by previous work(*17*). At small deposition thicknesses LCO grows as isolated islands (at larger thickness these islands coalesce into films) with either a (001) or (104) orientation on $SrTiO_3$(111) and $SrTiO_3$(001) oriented substrates, respectively. Transmission electron microscopy of the islands and the dependence on the substrate can be found in the supplementary text. As depicted in the schematic in Figure 1a, an ensemble of islands (on the order of 1×10^8 over a 0.242 cm^2 area) were electrochemically cycled in a three-electrode setup consisting of 1M $LiClO_4$ in propylene carbonate and Li foil counter and reference electrodes. Figure 1a is a plot of cyclic voltammetry of a Li_xCoO_2(104) with ~100 nm thick islands taken at 0.5 mV/s. Peaks are observed at 3.9 V with respect to Li/Li+ which is consistent with the presence of a two-phase region in which the equilibrium potential is flat. The sharpness of the peaks indicate excellent crystallinity of the material and the weaker satellite peaks are consistent with other epitaxial $LiCoO_2$. While the substrate induces some strain in the islands, the electrochemical cycling remained unaffected as observed previously (*17*). The islands were galvanostatically charged to a fraction of roughly x = 0.85 in Li_xCoO_2 based upon the reversible capacity of the first cycle and expected volume of the islands measured through AFM. Due to the difference in charge transfer resistances of the (104) and (001), the end voltage varied between 3.9-4.1 V depending on the sample (see supplementary information). As established previously, at x = 0.85 there is a similar fraction of α- and β-phases across an ensemble of particles(*6*).

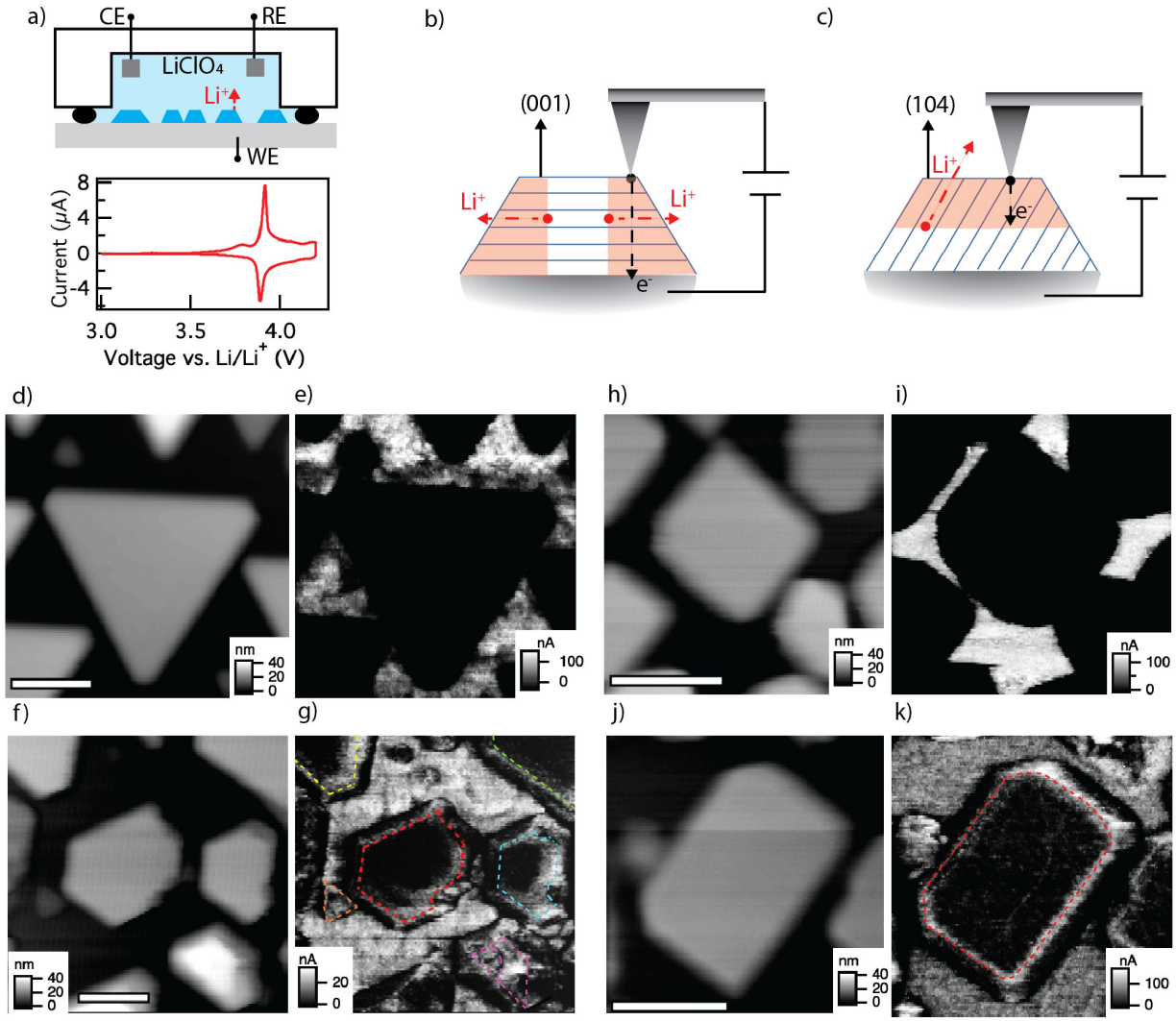

Figure 1. c-AFM of epitaxial LCO islands. (a) Cartoon depicting the experimental setup wherein islands (dark blue) are electrochemically cycled in electrolyte (light blue) that is encapsulated by a o-ring sealed chamber. Cyclic voltammogram of (104) oriented islands with a peaks at +3.9 V vs. Li/Li$^+$ (bottom). After electrochemical delthiation to x=0.85, the (001) and (104) oriented islands are imaged by c-AFM as depicted in the schematic in (b) and (c), respectively. Here, the islands are depicted in cross section with the intercalation planes as blue lines and Li movement indicated by red arrows. The white and red shaded area are indicating the α and β phases, respectively. Topographic and c-AFM images of (001) islands before and after delithiation are depicted in (d, e) and (f, g), respectively. Topographic and c-AFM images of (104) islands before and after delithiation are depicted in (h, i) and (j, k), respectively. The dashed colored lines demarcate the top facet surfaces of the islands. All scale bars correspond to 100 nm distance.

c-AFM was used to characterize the surface of the islands before and after electrochemical cycling in pure Ar environment (< 0.1 μPa/Pa of O_2 and H_2O). As depicted in the schematic in Fig. 1b, c-AFM measures the local electronic current through the surface by using an ammeter in-series with a conductive probe tip and a voltage bias circuit. All images were taken at a bias voltage of 0.75V (or less) to prevent significant movement of lithium due to large electric fields. Topography and current images of the (001) oriented islands taken before cycling are shown in Fig. 1d, e respectively. The metallic $SrRuO_3$ underlayer is found to be conductive between the islands. All island facets are found to be insulating, which is expected for stoichiometric $LiCoO_2$. This was also observed in c-AFM data of (104) oriented islands shown in Fig. 1h, i.

Fig. 1f,g are c-AFM images from the same (001) oriented sample as Fig. 1d,e post delithiation. From the c-AFM topography and error signal images we identify the (001) facets and have outlined them with colored dashed lines in the current image in Fig. 1g. We observe three distinct regions of current across the island surfaces: region 1) high current regions are observed on the (001) facet extending from the edges a roughly equal distance into the island 2) a low current region is observed at the island centers and region 3) a high current is observed where the facets meet at the island edges. Critically, we observe that region 1 extends a roughly uniform distance ~20 nm into island from most of the edges. This is most clearly observed in the red and cyan islands.

We attribute the regions 1 and 2 to the previously observed insulating and conducting α and β phases, respectively(*9*). The conductive β phase has c-axis lattice increase between ~1-1.50% over $0.75<x<0.94$ and has been studied in bulk extensively. The observation that the

conductive phase extends from the island edges a relatively uniform distance into the particle is attributed to diffusion as illustrated by the schematic in Fig. 1b. At low current charging rates, nucleation at surfaces can lead to intercalation waves or moving phase-boundaries that propagate inwards as the particle changes composition(*18*). Since lithium diffusion is favorable within the planes defined by the CoO_2 layers (red arrows), intercalation proceeds from the island edge. It is important to note that we observe this phase boundary *ex-situ* and perpendicular the (001) planes after cycling. Phase field modeling by Nadkarni *et. al*. found that the lowest energy configuration is for the phase boundary to exist parallel to the (001) planes(*5*), in which case the phase boundary would not be observed. This suggests that the islands exist in a kinetically arrested state that is preserved after cycling rather than relaxing to the lowest energy configuration.

Terracing or step edges within the islands further suggest diffusion-mediated phase segregation. For example, the magenta island in Fig. 1g has a terraced structure with two (001) facets and a much smaller area than the rest of the islands. The surface of this island becomes almost entirely conductive, suggestive of multiple intercalation fronts. The smallest island shown in orange is also nearly entirely conductive. The disproportionately large share of metallic phase existing in these islands suggests that, in isolation, they would exist in a state of charge that is quite different than what is assumed from the ensemble of islands. This has interesting ramifications for the ensemble state of charge as measured through a potentiostat and we discuss such effects later.

To further investigate kinetically arrested states, we cycled (104) oriented particles to a similar filling fraction $x \approx 0.85$. In the c-AFM current data in Fig. 1k, we observe two distinct regions of current: a low-current region which extends all the way to the (104) facet edges and

thin regions with higher current where the facets meet at the island edges. We did not observe a clear phase boundary on the top of the (104) oriented islands as was observed with the (001) oriented islands. An explanation for this is depicted in the schematic in Fig. 1c. Here, the Li-diffusion planes confine the conductive phase boundary parallel to the surface leaving the top of the island conductive and the bottom insulating. This prevents tip current flowing through the island due to an insulating region below. This further suggests a kinetically arrested state (as seen with (001) islands). In contrast, the lowest energy configuration would have conductive and insulating phases segregate in plane across the island.

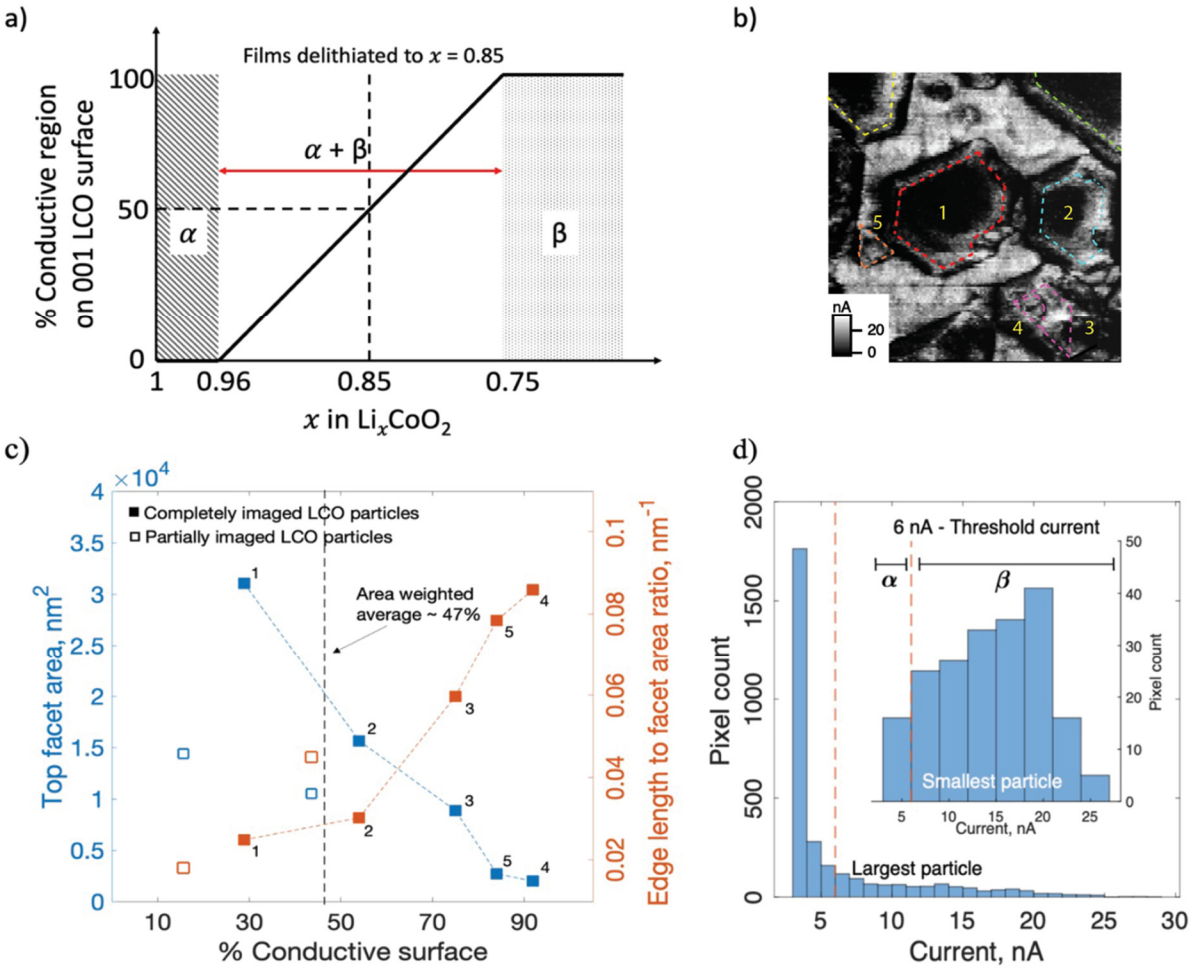

Figure 2. a) Expected phase behavior of bulk LCO particles as a function of x in Li_xCoO_2. For x = 0.85, the percentage of conductive region on the particle top facet imaged should be 50%, b) Imaged LCO particles with top facets shown by dashed colored lines and numbered as 1,2,3,4, and 5. The two particles on the top left and top right were partially imaged, and the terraced LCO particle on the bottom right consists of two smaller particles of different thicknesses: 4 (lower terrace) and 5 (upper terrace), c) Panel showing the % conductive surface for each particle imaged as a function of top facet area and edge length to surface area ratio. The dashed lines between the solid points are simply connectors. The area-weighted average of the % Conductive surface for fully imaged particles 1 to 5 is shown with a vertical dashed line. d) Further details on the current thresholding used in our image analysis. Number of conductive and non-conductive pixels in the largest (Particle 1, main plot) and smallest (Particle 4, subplot) particles based on the threshold current of 6 nA.

To quantify the phase behavior in individual particles, we carried out image analysis on the c-AFM data for delithiated 001 particles. The deflection and c-AFM data were used in conjunction to identify island top facet edges and calculate the percentage of conductive phase for each island. As shown in Fig.2a, assuming the particles behave as bulk LCO, in the two-phase region of LCO between x =0.96 and x = 0.75, the delithiation to x = 0.85 should result in ~50% of the top facet area being conductive (i.e., β phase). The top facet edges are again shown with dashed color lines, and the particles are numbered, in Fig 2b. For our image analysis, we used a threshold current (see Fig 2d) to classify each pixel on the top surface as either conductive (for measured current > threshold current) or insulating (measured current < threshold current). The results of this analysis are shown in Fig 2c.

Our analysis on five LCO particles and two partially imaged LCO particles shows that the fraction of the top facet that is conductive correlates with particle size, with smaller particles having a higher fraction of conductive top facet. Also shown in Fig 2c is the area weighted average of the percent of conductive surface for the five fully imaged particles; the value is 47%. which is very close to the expected average value of 50% in the simple schematic of Figure 2a. We note that our results here are sensitive to the current threshold we chose (6 nA), as shown in Fig 2d, and are likely also sensitive to the number of particles analyzed (we used a sample size of 5). Given the strong sensitivity of the electronic conductivity of LCO in the $1<x<0.96$ region (>100x variation) and the role of contact resistance, we assess this threshold to be reasonable. The observation in Fig. 2c that smaller particles have a higher fraction of conductive facet may be due to several effects. First, assuming each particle has the same delithiation kinetics, because the delithiation of the (001) particles occurs on the sides, smaller particles should have a higher delithiated fraction (at least within the two-phase region where the equilibrium potential is

flat). In addition, measurements of electronic conductivity vs. lithiation for LCO of different sizes could help further explore whether size-dependent thermodynamic and transport properties contribute to our observations here.

Next, we discuss region 3, a conductive, ~10 nm wide region about where the island facets meet. Although this region appears at the island edges, we find this region to be distinct from region 1 (which was found to extend inwards). The effect is most clearly visible in Fig. 1k, where the top (104) facet meets the side facets (indicated by dashed red line): a thin conductive line is observed with roughly 10 nm width about the dashed line (or roughly the tip diameter). The effect is also seen at the island corners, where the facets on the island sides meet each other. Here, the conductive region extends all the way to the substrate, although regions thicker than 10 nm are visible there as well. These regions cannot be explained by a diffusion-limited phase boundary, and they cannot be easily attributed to α or β phases observed in bulk. Previously, Okubo *et. al*. used electron energy loss spectroscopy (EELS) in a transmission electron microscope to observe surface regions in LCO crystallites where the average Co oxidation state was 2.7^{+}(*19*). These regions measured approximately 3 nm in width and were interpreted to have excess Li, or $Li_{1+\delta}CoII_{\delta}CoIII_{1-\delta}O_2$. If this is indeed the case, the local enhancement in Li would dope the LCO n-type, leading to enhanced conductivity. As with Okubo et. al., we observe the high conductance surfaces at particle edges.

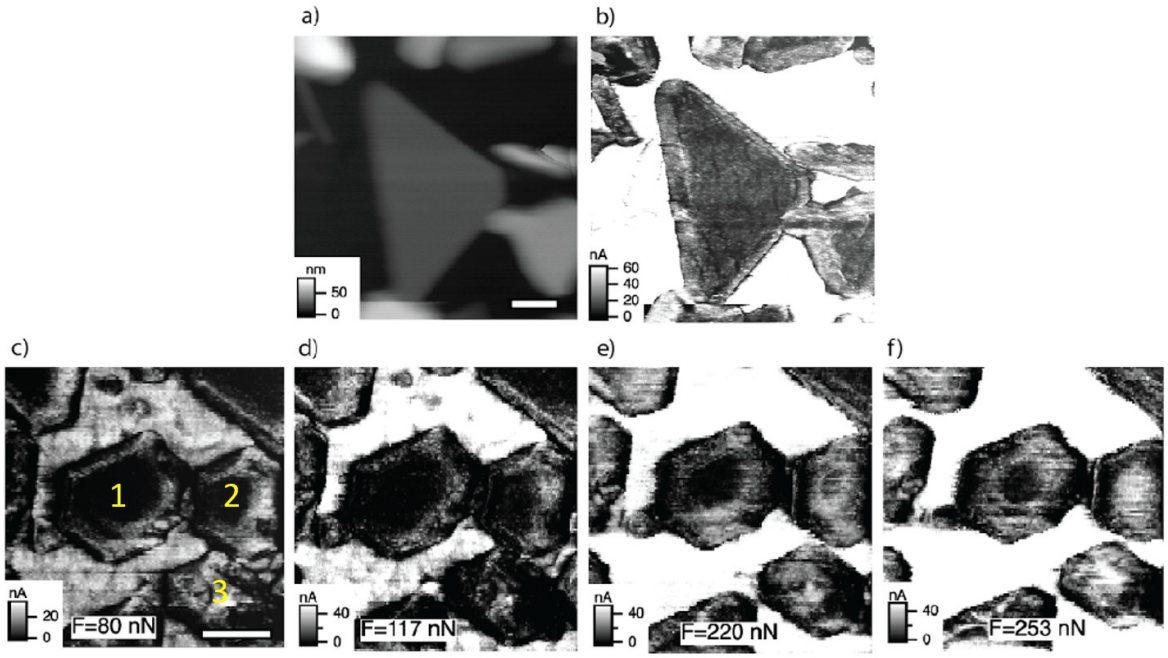

Figure 3. Strain and surface effects in epitaxial LCO islands. Panel (a) and (b) are drift and tip corrected topography and current images of a 14 nm thick island with (104) orientation (center) cycled to x≈0.85. A lamellar-like pattern is observed at the surface of the particle. (c) – (f) C-AFM current images of 001 oriented islands at 80 – 253 nN of tip force, respectively. All scale bars correspond to 100 nm length.

While most (104) oriented islands exhibited insulating behavior, we found thinner islands with different phenomena. Figure 3a, b are c-AFM data from a 14 nm thick (104) oriented island post-electrochemical cycling to x≈0.85 (at center). The images are drift corrected to accurately display the particle geometry (for more information see the supplementary text). We again observe a conductive background and find that the island is significantly more resistive. Across the island itself, we observe distinct regions of high- and low-current, similar to what was found with (001) oriented particles. However, in this case we find that the phases have segregated in a striping pattern with an average pitch of approximately λ=30 nm. It is known that phase separation can lead to spontaneous formation of domains and that periodic structures can emerge due to the competition between chemical free energy, composition gradients and stress.

Previously, it was shown that $LiFePO_4$ battery particles exhibit phase segregation in a similar striped pattern(*20*). Cogswell *et. al*. explained the striping observed in $LiFePO_4$ as a stable equilibrium for particles with a finite size and phase field modeling reproduced the characteristic wavelength over which stripes were observed which scales as $\lambda \propto \sqrt{L}$, where L is the scale of the particle(*21*). Such phenomena could exist in (104) particles, but this does not necessarily explain why this island exhibits striping whereas thicker islands were found in a kinetically arrested state.

One explanation for the observed striping pattern is a surface-dominated spinodal decomposition wherein the surface energy dictates phase morphology. Since intercalation occurs primarily along the (104) direction normal to the surface it would make sense for this surface energy to play a dominant role in thinner particles. For example, surface-coherent spinodal decomposition (SCSD) is predicted to occur in nanoscale particles with high surface area to volume ratios and where coherent surface modes dominate(*22*). Tang *et. al.* predict a striping pattern for particles with a similar wavelength (λ ~30nm) over a particle with similar widths (~250nm), although it is expected that for SCSD the wavelength λ should be independent of particle size(*22*).

Finally, we discuss force-induced metal insulator transitions observed in the case of (001) oriented islands. The c-AFM images are in Fig. 3 c-f, and are taken on the same island as in Fig. 1 f), g) but over a series of tip-sample forces ranging from 80 - 253 nN. Forces in this range will induce >1GPa stress in the contact region when assuming the stress distribution is uniform and the contact area is 100 nm^2. Considering particles 1, 2, and 3 in panels c to f, we generally observe increasing current with increasing force. At a more detailed level, we also observe

qualitatively different trends in the current within islands 1 to 3, for example between Fig. 3d and Fig. 3e. For island 1, moving from d) to e) shows a general increase in current throughout the island. On the other hand, for island 3, moving from d) to e) shows that the center comes to have a significantly higher current than the other regions of the particle. We identify several factors that may contribute to the interpretation of the data here and in future such experiments. First, the partial molar volume of Li in Li_xCoO_2 is negative for approximately $0.6<x<0.95$(*23*), which could mean that when the volume is reduced (by applying strain), the local Li concentration should increase (within this range of x values), which in turn should reduce the conductivity of the LCO. It may also be the case that at higher strain in this experiment the tip could force the lithium (in lithium-rich regions) under the tip to be pushed into lower concentration lithium regions, making the region just under the tip metallize and possibly inducing a phase transformation from α to β. In this case one would expect the entire island to become conductive once the force threshold for displacement is reached. Second, the geometry and mechanical boundary conditions on the islands affect their elastic deformation. In particular, boundary regions are closer to the mechanically free islands sides, which means they may deform more easily and provide better contact with the AFM tip, which in turn affects the measured current flow in the experiment. Finally, there may be dynamic effects present in these measurements that experiments at different scan rates may reveal although we did not investigate this effect. This may be important if Li diffusion takes place beneath the AFM tip.

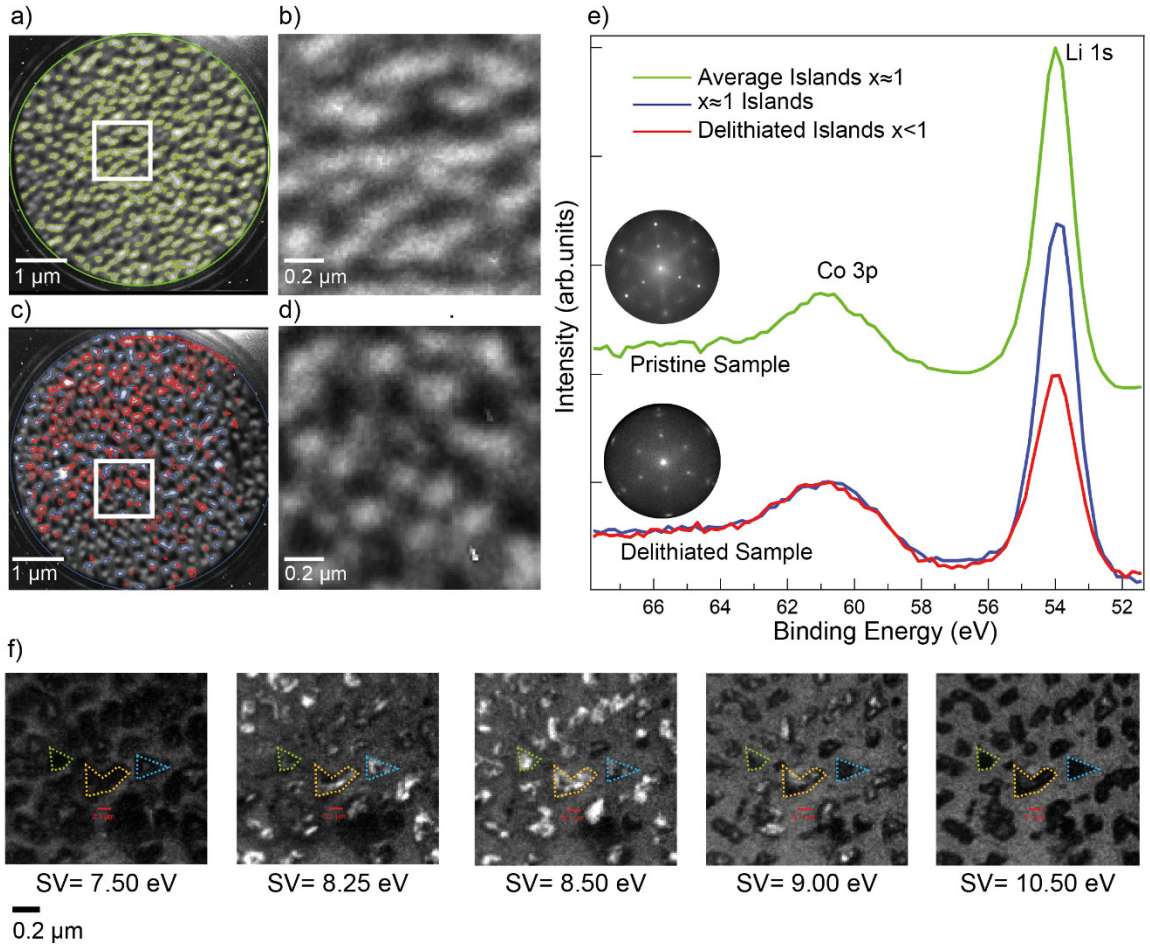

Figure 4. PEEM / LEEM data of LCO (001) islands grown on STO/SRO. PEEM image over Li 1*s* energy range at a 5 micron (a) and 1 micron field of view (b) obtained from the white square defined region in (a). Subsequent PEEM image after sputter / anneal delithiation process at 5 micron (c) and 1 micron (d) field of view from the white square defined region in (c). (e) Integrated Co 3*p* and Li 1*s* peaks for pristine case (green) delithiated case (blue) and over selected islands which showed strong delithiation outlined in red in (c). LEED insets of the pristine and sputtered samples are also shown in panel (e) . A series of LEEM images at a series start voltages (labeled SV) is shown in (f) to highlight the topography, scale bar below first panel indicates the scale for all images in (f). For PEEM spectra a photon energy of 150 eV was used.

While conductive AFM may provide insights into a few particles, it is desirable to acquire larger statistics. Photoemission spectroscopy and low energy electron microscopy can

resolve local chemical information across a larger number of particles due to non-rastering imaging and a larger field of view(*24*). Fig. 4 summarizes the results of our imaging in both PEEM and electron emission (LEEM) modes of similarly grown LCO (001) islands to those analyzed by c-AFM. Beginning with a pristine sample, a good homogeneity between islands is observed. From the Li 1s / Co 3p peaks ratio we identify stoichiometric Li_xCoO_2 (x=1) (green outlined regions in Fig4.a)). This identification is further confirmed using island shapes (with AFM reference images) and the valence band shape in those regions. The delithiation procedure involves cycles of gentle Ne^+ sputtering and annealing at 500 °C in oxygen atmosphere ($P_{O2}=5\times10^{-6}$ mbar). This treatment delithiates the surface layers of the islands (due to the Li higher sputtering yield), while preserving the surface quality and crystallinity as it is seen in the LEED patterns (see insets of panel 4e)). After the delithiation process, there is preference for certain islands to become delithiated, increasing the inhomogeneity between islands, with some islands having a more metallic character and a lower lithium to cobalt ratio. It is important to note that no such inhomogeneity is observed before the delithiation process. Li deficient islands make up around 50% for small field of view (1 μm^2) regions. An example is marked with white a square in Figure 4 (c) and has x=0.6 ±0.3 in comparison with the stoichiometric islands (green selection in Figure 4(a). This is consistent with the β phase segregated to the very top surface. To avoid experimental errors due to the limited resolution in the edge of the islands, we have assigned as β phase islands as only those islands with a valence band of clear metallic character and lower Li 1s / Co 3p peaks ratio in their center. Note the high variability in this group of delithiated islands, where x=0.6 denotes the average. Since the other regions exhibit ratios close to x=1.0 and a more insulating behaviour, we assign them as α phase. It is important to emphasize that, in the pristine case, no such group of consistently delithiated and conductive

(less charge shift) islands is observed. The study of individual islands suggests that no border effects or inhomogeneity within individual islands is found using PEEM, as we observed following electrochemical delithiation, at least up to the experimental resolution of PEEM (around 20 nm).

The results of the sputter/anneal delithiation process provide a useful comparison to the electrochemically delithated samples. The lack of preferential delithiation from the edge (as seen with AFM) is consistent with the sputter/anneal process as opposed to intercalation from the planes. The anneal process raises the temperature such that the surface has enough thermal energy to evolve towards thermodynamic equilibrium rather than having any kinetic metastability. Therefore, the fact that the system evolves towards certain particles in a more delithiated state suggests that there is a preference towards such an equilibrium thermodynamically(*5*). Finally, we note that imaging of electrochemically delithiated samples using photoelectron spectroscopy/LEEM is a promising avenue for future work for comparing larger scale statistics to the nanoscale features observed with c-AFM.

Next, we discuss the implications of our results to battery, electrocatalysis and ECRAM applications of LCO. First, our results resolve an outstanding question posed by Nadkarni *et. al*. as to whether LCO sits in a kinetically arrested state due to diffusional anisotropy or if it relaxes back to the lowest energy state. Regardless of particle orientation we find that at low charging rates (C/10) the kinetically arrested state is observed. We find this kinetically arrested state was maintained for several days past delithiation but we did not investigate longer metastability. This perhaps has the most important ramifications for ECRAM in which the phase morphology could have significant impact on the macroscopic conductance state. For example, an insulating phase

boundary near a contact electrode could dominate the device properties (i.e. contact resistance). This boundary would likely remain static over the course of at least several days and potentially much longer given the macroscopic device retention measured in our earlier work(*4*). For memory it is desirable for the kinetically arrested state to either be permanent or quickly decay to the lowest energy configuration. Gradual decays are not desirable as these contribute to drift such as observed in chalcogenide glass memory(*25*). Future work will have to determine whether solid-solutions observed by Flores *et. al.* will relax to the lowest energy configurations predicted by Nadkarni and over what timescale the relaxation occurs, with faster timescales being far more desirable.

Another important finding are islands existing with different fractions of lithium content that contribute to a single microstate of charge as illustrated in Fig. 2 . Although not surprising, this has implications to both battery and ECRAM cells. For example, smaller particles with high metallicity may dominate charging characteristics, especially at intermediate charging rates between solid solution and two-phase coexistence. An open question is whether some particles enter a solid solution phase while others remain segregated at the tails of the coexistence region.

With respect to electrocatalysis, recent studies indicate that delithiated LCO exhibits substantial oxygen evolution reaction (OER) activity(*26*). Furthermore, LCO nanoparticles with various surface orientations exposed to electrolyte exhibited considerably higher activity compared to LCO nanosheets with predominantly basal (001) surface exposure(*27*). Theoretically, surfaces with the (110) and the (012) orientations were predicted to exhibit the highest activity. These results are consistent with our local conductance measurements indicating that while the edges become electronically conducting following delithiation, the basal planes remain largely insulating. We propose that LCO nano-islands with precisely tuned orientation and dimensions,

coupled with spatially resolved conductance measurements, represent an excellent opportunity to quantitatively relate specific surfaces with electrocatalytic activity.

Finally, we discuss the implications of force induced metallization and transformation from α to β. This is an especially important consideration for solid-state systems that undergo significant mechanical stress due to solid-electrolyte overlayers. Stress points, independent of particle size, may metallize more quickly than is predicted from existing charging models and therefore dominate the electrochemical activity.

Our results point more broadly to nanoscale effects that cannot be predicted from bulk phase diagrams to capture device performance. Interplay between diffusion, strain and electron correlation can lead to unexpected phase morphology depending on dimensionality and charging rates. We have only scratched the surface in understanding these effects in LCO and further investigations are required to understand precisely how the behavior extends to ensembles of particles (i.e. how they contribute to macroscopic state of charge) especially at transition points in the bulk phase diagram. (i.e. phase coexistence to solid solution crossover). Finally, we expect these phenomena to be observed in other correlated oxides of interest such as $LiFePO_4$, $NaCoO_2$, etc. Capturing these emergent nanoscale phenomena is critical to constructing models that can guide improvements in battery, electrocatalyst and ECRAM performance.

METHODS

Electrochemical cycling

The substrates were mounted electrically and mechanically to a stainless steel plate using silver paste. An o-ring was used to confine a volume of electrolyte in contact with the center of the

substrate. A mixture of 1M $LiClO_4$ in propylene carbonate was used as the electrolyte. Electrical contact was made to the metallic $SrRuO_3$ underlayer using silver paste or copper tape at the edges of substrate and away from the electrolyte. Cyclic voltammetry was performed between 3-4.2 V with respect to Li or a $LiFePO_4$ counter electrode and a Li reference electrode was used to monitor the potential. For the conductive AFM measurements, the islands were galvanostatically charged at C/8 until approximately 0.15 mols of Li were removed, as calculated from the measured volume of the islands. All testing and assembly was conducted in an Ar glovebox (<1ppm H_2O and O_2).

Pulsed laser deposition

Pulsed laser deposition of LCO was carried out on a stoichiometric $LiCoO_2$ target and a Li_2O target at a duty cycle of 25:1 and at a rate of 5Hz and fluence of 3.6 J cm^{-2}. Growth was carried out at a temperature of 650C and in an oxygen partial pressure of 26.6 Pa. The SrTiO (100) subtrates were prepared using a buffered oxide etch with a post annealing at 900C in air.

Conductive AFM

Unless otherwise stated, the probe force was approximated at 80 nN based upon the cantilever spring constant and measured deflection. All images were taken with a ballast resistor of 5 MΩ in series with the ammeter circuit to prevent overcurrent through the C-AFM tip. The c-AFM images were recorded using doped diamond tips with a radius of curvature of < 5 nm (Adama AD-2.8-SS) or platinum silicide tips (PtSi FM) with a radius of curvature of < 25 nm.

SPELEEM data

The SPELEEM data were taken at Nanospectroscopy beamline of the Elettra syncrotron in Trieste, Italy. The beamline end-station is equipped with an low-energy electron microscope with hemispherical energy analyser (SPELEEM III, Elmitec GmbH). To probe the specimen surface,

the microscope can use either electrons (LEEM operation) or soft x-rays in the range 25-1000 eV (PEEM operation). LEEM allows applications such as real-time imaging of the surface and micro-spot diffraction measurements. When using the beamline photons, the SPELEEM microscope can peform x-ray absorption spectroscopy or x-ray photoelectron spectroscopy with lateral resolution better than 30 nm can record selected-area x-ray absorption spectra or spatially resolved photoemission images.

Sputtering procedure

Physical delithiation was done by Ne+ sputtering under controlled conditions (ion energy of 600 eV, sample current of 0.5 μA) in 5 minute steps. After every sputter cycle a gentle annealing of 10 min at 500 C was performed to improve the surface crystallinity as checked by LEED.

Image Analysis

The deflection data was first denoised by using a low-pass Butterworth filter with a cutoff frequency of 40 Hz. The data was converted to a grayscale image, where edges were identified as grayscale values below 0.4 and above 0.55. To segment the individual particles, graph cut method was used in the image segmentation toolbox in MATLAB, which uses the active contour algorithm to locate particle boundaries. This segmentation was used to create masks corresponding to the top facet area of each particle. The total number of pixels in the masks were counted to represent the area of particles (in pixels). These masks were then applied to the c-AFM current image (converted to a grayscale image) to segment the individual particles in the c-AFM image. The c-AFM current data was corrected for a special gradient that likely originates from data acquisition in contact mode. The current cutoff grayscale value was 0.15 (~6 nA); all pixels with grayscale values greater than 0.15 were classified as conductive. The fraction of the conductive region was determined by dividing the number of conductive pixels by the total number of pixels in the masked region (i.e,

the top facet of each particle). The edge length to top facet surface area pixel ratio, indicating the surface to volume ratio of a particle, was determined by taking the ratio of the number of pixels on the edge of each particle's top facet to the number of pixels on the surface of the facet. An area-weighted average was calculated for five out of the seven particles analyzed. The two partially imaged particles were not included in the averages.

ACKNOWLEDGEMENTS

E.J.F. and A.A.T. were supported by the Sandia Laboratory-Directed Research and Development (LDRD) Program. Sandia National Laboratories is a multimission laboratory managed and operated by National Technology and Engineering Solutions of Sandia, LLC., a wholly owned subsidiary of Honeywell International, Inc., for the US Department of Energy's National Nuclear Security Administration under contract DE-NA-0003525. The views expressed in the article do not necessarily represent the views of the US Department of Energy or the United States Government. Analysis and modeling of the c-AFM experiments was carried out by B.B, Y.S., and P.A. and supported by the U.S. Department of Energy, Office of Science, Office of Basic Energy Sciences under Award Number DE-SC0021070.

C.P. thanks the academic stay support of the mobility program "Salvador de Madariaga" (MICINN) under Ref. PRX19/00486. M.A.G.B. and A.M. thank Ministerio de Ciencia e Innovación (project PID2020-117024GB-C43) and Comunidad de Madrid (project S2108–NMT4321) for financial support. C.P., E.S., E.V., P.S. and E.G.M. thank Ministerio de Ciencia e Innovación (grant FIS2017-82415-R), "María de Maeztu" Programme for Units of Excellence in R&D (CEX2018-000805-M)), and UE M-ERA.NET 2018 program/Agencia Estatal de Investigación (AEI) under StressLIC Project (grants nr. PCI2019-103604 and PCI2019-103594). The research leading to this result has been supported by the project CALIPSOplus under Grant

Agreement 730872 from the EU Framework Programme for Research and Innovation HORIZON 2020.

REFERENCES

1. J. Lim *et al.*, Origin and hysteresis of lithium compositional spatiodynamics within battery primary particles. *Science* **353**, 566-571 (2016).
2. Z. W. Seh *et al.*, Combining theory and experiment in electrocatalysis: Insights into materials design. *Science* **355**, (2017).
3. J. Wang *et al.*, Redirecting dynamic surface restructuring of a layered transition metal oxide catalyst for superior water oxidation. *Nature Catalysis* **4**, 212-222 (2021).
4. E. J. Fuller *et al.*, Li-Ion Synaptic Transistor for Low Power Analog Computing. *Adv Mater* **29**, (2017).
5. N. Nadkarni, T. Zhou, D. Fraggedakis, T. Gao, M. Z. Bazant, Modeling the Metal–Insulator Phase Transition in Li_xCoO_2 for Energy and Information Storage. *Advanced Functional Materials* **29**, (2019).
6. K. Mizushima, P. C. Jones, P. J. Wiseman, J. B. Goodenough, LixCoO2 (0<x<-1): A new cathode material for batteries of high energy density. *Materials Research Bulletin* **15**, 783-789 (1980).
7. A. Van der Ven, M. K. Aydinol, G. Ceder, G. Kresse, J. Hafner, First-principles investigation of phase stability inLixCoO2. *Physical Review B* **58**, 2975-2987 (1998).
8. C. A. Marianetti, G. Kotliar, G. Ceder, A first-order Mott transition in LixCoO2. *Nat Mater* **3**, 627-631 (2004).
9. A. Milewska *et al.*, The nature of the nonmetal–metal transition in LixCoO2 oxide. *Solid State Ionics* **263**, 110-118 (2014).
10. M. Okubo *et al.*, Nanosize effect on high-rate Li-ion intercalation in LiCoO2 electrode. *J Am Chem Soc* **129**, 7444-7452 (2007).
11. N. C. Bartelt *et al.*, Simple Stochastic Model of Multiparticle Battery Electrodes Undergoing Phase Transformations. *Physical Review Applied* **10**, (2018).
12. Y. Li, W. C. Chueh, Electrochemical and Chemical Insertion for Energy Transformation and Switching. *Annual Review of Materials Research* **48**, 137-165 (2018).
13. Y. Li *et al.*, Current-induced transition from particle-by-particle to concurrent intercalation in phase-separating battery electrodes. *Nat Mater* **13**, 1149-1156 (2014).
14. X. Zhu *et al.*, Direct observation of lithium-ion transport under an electrical field in LixCoO2 nanograins. *Sci Rep* **3**, 1084 (2013).
15. Y. H. Xu *et al.*, In situ Visualization of State-of-Charge Heterogeneity within a LiCoO2 Particle that Evolves upon Cycling at Different Rates. *Acs Energy Letters* **2**, 1240-1245 (2017).
16. A. J. Merryweather, C. Schnedermann, Q. Jacquet, C. P. Grey, A. Rao, Operando optical tracking of single-particle ion dynamics in batteries. *Nature* **594**, 522-528 (2021).
17. S. Takeuchi *et al.*, Epitaxial LiCoO2 films as a model system for fundamental electrochemical studies of positive electrodes. *ACS Appl Mater Interfaces* **7**, 7901-7911 (2015).
18. E. Flores, N. Mozhzhukhina, U. Aschauer, E. J. Berg, Operando Monitoring the Insulator–Metal Transition of LiCoO2. *ACS Applied Materials & Interfaces* **13**, 22540-22548 (2021).
19. M. Okubo, J. Kim, T. Kudo, H. Zhou, I. Honma, Anisotropic Surface Effect on Electronic Structures and Electrochemical Properties of LiCoO2. *The Journal of Physical Chemistry C* **113**, 15337-15342 (2009).
20. G. Chen, X. Song, T. J. Richardson, Electron microscopy study of the LiFePO4 to FePO4 phase transition. *Electrochemical and Solid State Letters* **9**, A295 (2006).

21. D. A. Cogswell, M. Z. Bazant, Coherency strain and the kinetics of phase separation in LiFePO4 nanoparticles. *ACS nano* **6**, 2215-2225 (2012).
22. M. Tang, A. Karma, Surface modes of coherent spinodal decomposition. *Physical review letters* **108**, 265701 (2012).
23. R. Koerver *et al.*, Chemo-mechanical expansion of lithium electrode materials – on the route to mechanically optimized all-solid-state batteries. *Energy & Environmental Science* **11**, 2142-2158 (2018).
24. A. Locatelli, L. Aballe, T. O. Mentes, M. Kiskinova, E. Bauer, Photoemission electron microscopy with chemical sensitivity: SPELEEM methods and applications. *Surface and Interface Analysis* **38**, 1554-1557 (2006).
25. G. P. Tiwari *et al.*, Structural relaxation in metallic glasses. *Materials Science and Engineering: A* **304-306**, 499-504 (2001).
26. Z. Y. Lu *et al.*, Electrochemical tuning of layered lithium transition metal oxides for improvement of oxygen evolution reaction. *Nature Communications* **5**, (2014).
27. Z. Y. Lu *et al.*, Identifying the Active Surfaces of Electrochemically Tuned LiCoO2 for Oxygen Evolution Reaction. *Journal of the American Chemical Society* **139**, 6270-6276 (2017).